ADVANCED MATERIALS
www.advmat.de

Direct Pyrolysis of Supermolecules: Ultrahigh Edge-Nitrogen Doping Strategy of Carbon Anodes for Potassium-Ion Batteries

Wenli Zhang, Jian Yin, Minglei Sun, Wenxi Wang, Cailing Chen, Mustafa Altunkaya, Abdul-Hamid Emwas, Yu Han, Udo Schwingenschlögl, and Husam N. Alshareef*

Most reported carbonaceous anodes of potassium-ion battery (PIB) have limited capacities. One approach to improve the performance of carbon anodes is edge-nitrogen doping, which effectively enhances the K-ion adsorption energy. It remains challenging to achieve high edge-nitrogen doping due to the difficulty in controlling nitrogen dopant configuration. Herein, a new synthesis strategy is proposed to prepare carbon anodes with ultrahigh edge-nitrogen doping for high-performance PIB. Specifically, self-assembled supermolecule precursors derived from pyromellitic acid and melamine are directly pyrolyzed. During the pyrolysis process, the amidation and imidization reactions between pyromellitic acid and melamine before carbonization enable the successful carbonization of pyromellitic acid-melamine supermolecule. The obtained 3D nitrogen-doped turbostratic carbon (3D-NTC) possesses a 3D framework composed of carbon nanosheets, turbostratic crystalline structure, and an ultrahigh edge-nitrogen-doping level up to 16.8 at% (~~73.85~~% of total 22.8 at% nitrogen doping). These features endow 3D-NTCs with remarkable performances as PIB anodes. The 3D-NTC anode displays a high capacity of 473 mAh g^{-1}, robust rate capability, and a long cycle life of 500 cycles with a high capacity retention of 93.1%. This new strategy will boost the development of carbon anodes for rechargeable alkali-metal ion batteries.

The increasing demand for sustainable electricity from intermittent renewable resources (wind, solar, tide, etc.) has triggered an urgent need for low-cost electrochemical energy storage systems.[1] Considering the limited lithium content in the earth's crust,[2] and significantly more abundant potassium resources, similar to sodium,[3] potassium-ion battery (PIB) has become an increasingly important next-generation electrochemical energy storage device.[4,5] PIB has a similar "rocking-chair" operating principle with lithium-ion batteries (LIB) and sodium-ion batteries (SIB). However, due to the larger radius of potassium atom (1.38 Å) compared with that of lithium (0.68 Å) and sodium (0.97 Å),[6] most anode materials used in LIBs and SIBs suffer from inferior performances when used as PIB anodes,[7,8] such as hard carbon,[9] silicon,[8] and various alloying anodes.[7] Fortunately, some amorphous carbonaceous materials show higher potassium-ion storage capacities than their sodium-ion storage capacities.[10] This phenomenon is attributed to the fact that potassium ion can intercalate into graphitic carbon nanodomains (GNDs) with a (002) interlayer spacing of 3.35 Å.[11–14] In contrast, sodium ion can only intercalate into GNDs with interlayer spacings >3.7 Å in carbonate-based electrolytes.[15] As a vital family of anode materials for PIB, carbonaceous materials hold great potential towards commercialization due to their abundance, nontoxic nature, and low energy/chemical consumption.[16,17] Given the limited potassium-ion storage capacities of graphite (278 mAh g^{-1}),[12,18,19] and hard carbon (<300 mAh g^{-1}),[9] their poor cycling stabilities, and inferior rate performances in carbonate-based electrolytes, various low-temperature-annealed amorphous carbons with expanded interlayer spacings have been developed as high-performance PIB anodes.[20–24] Nitrogen doping is an effective strategy to promote the potassium-ion storage capability of carbonaceous materials.[25–29] Generally, nitrogen dopants are classified into pyridinic, pyrrolic, and graphitic nitrogens. The graphitic nitrogen dopant, surrounded by three carbon atoms, is a nitrogen atom that replaces one carbon atom in an in-plane graphene hexagonal structure.

Dr. W. Zhang, Dr. J. Yin, Dr. M. Sun, W. Wang, Prof. U. Schwingenschlögl, Prof. H. N. Alshareef
Materials Science and Engineering
Physical Science and Engineering Division
King Abdullah University of Science and Technology (KAUST)
Thuwal 23955-6900, Saudi Arabia
E-mail: husam.alshareef@kaust.edu.sa
Dr. C. Chen, Prof. Y. Han
Advanced Membranes and Porous Materials Center
Physical Science and Engineering Division
King Abdullah University of Science and Technology (KAUST)
Thuwal 23955-6900, Saudi Arabia
M. Altunkaya, Dr. A.-H. Emwas
Core Labs
King Abdullah University of Science and Technology (KAUST)
Thuwal 23955-6900, Saudi Arabia

The ORCID identification number(s) for the author(s) of this article can be found under https://doi.org/10.1002/adma.202000732.

DOI: 10.1002/adma.202000732

Edge-nitrogen dopants are pyridinic and pyrrolic nitrogens that are bonded by two adjacent carbon atoms while leaving itself on the edge of a GND. As demonstrated by computational and experimental methodologies, edge-nitrogen-induced defects are active sites for adsorbing potassium ions compared with graphitic-nitrogen-doped, and un-doped GNDs.[30–32] Unfortunately, most reported nitrogen-doped carbonaceous materials have low nitrogen doping levels <10 at% (a large portion is electrochemically inactive graphitic nitrogen)[33–37] that is too low to exert their potassium-ion storage capability. Some carbonaceous materials could achieve edge-nitrogen doping ratio of ≈90%,[38] but they possess a rather low nitrogen doping level of 4.32 at%. Carbonaceous materials with both high nitrogen doping levels and high edge-nitrogen doping ratios are significant to enhance the potassium-ion storage capacity of carbonaceous materials.

Herein, we present a new synthesis strategy of carbon anodes with ultrahigh edge-nitrogen doping level for high-performance PIB. In this strategy, we use pyromellitic acid (PMA) and melamine (MA) as monomers to realize ultrahigh edge-nitrogen doping in carbonaceous materials. Pure PMA and MA monomers cannot be carbonized because of sublimation and decomposition. On the contrary, the self-assembled PMA-MA supermolecule can be carbonized due to the pre-carbonization reactions of amidation and imidization between PMA and MA monomers. The amide and imide structures formed before carbonization greatly enhance the thermostability of PMA and MA, which enables the successful carbonization of PMA and MA. As a result, we obtained 3D nitrogen-doped turbostratic carbon (3D-NTC) with an ultrahigh edge-nitrogen doping level of 16.8 at%. This ultrahigh edge-nitrogen doping endows 3D-NTC with excellent performances as a PIB anode. Specifically, the 3D-NTC anode shows a high stabilized reversible capacity of 473 mAh g^{-1}, robust rate capability, and a long cycle life of 500 cycles with a high capacity retention of 93.1%. Furthermore, the high-performance 3D-NTC anode was assembled into a high-performance PIB using perylenetetracarboxylic dianhydride (PTCDA) as the cathode.

Figure 1a shows a schematic illustration of the synthesis of 3D-NTC. PMA and MA were used as precursors for the synthesis of 3D-NTC. PMA and MA first react in water and form self-assembled supermolecule (PMA-MA) crystals (Figure S1, Supporting Information) due to the strong hydrogen bonding between PMA and MA molecules.[39] The formation of PMA-MA supermolecule is demonstrated by X-ray diffraction (XRD) and Fourier transform infrared (FTIR) spectroscopy (Figure S2, Supporting Information). After a one-step pyrolysis process, the PMA-MA supermolecule was successfully carbonized into 3D-NTC. The 3D-NTC samples obtained at annealing temperatures of 750 and 900 °C are termed as 3D-NTC750 and 3D-NTC900, respectively.

Pure PMA cannot be carbonized since PMA sublimes at a temperature of ≈280 °C. Likewise, pure MA faces sublimation and decomposition at temperatures above ≈350 °C (Figure 1b). The MA molecules are polymerized into graphitic carbon nitride (g-C_3N_4) at temperatures around 500 °C.[40] Nevertheless, g-C_3N_4 fully decomposes at temperatures above 650 °C (Figure 1b). On the contrary, the PMA-MA supermolecule can be carbonized at high temperatures ranging from 400 to 1000 °C, as demonstrated by the increased thermostability through thermogravimetric analysis (TGA) (Figure 1b). The differential scanning calorimetry (DSC) curve shows three endothermic peaks at temperatures ranging from 100 to 350 °C. These three endothermic peaks belong to pre-carbonization processes. We tracked the pyrolysis behavior of the PMA-MA supermolecule by mass spectroscopy (MS). The release of NH_2 groups at 295 °C is ascribed to the partial sublimation or decomposition of MA molecule, while the release of CO_2 at 298 °C is ascribed to the partial sublimation or decomposition of PMA molecule (Figure 1c). MS spectra show three H_2O release peaks at 141, 236, and 295 °C, respectively (Figure 1c). The H_2O release peak at 141 °C results from the release of crystal water in PMA-MA supermolecules. The second (236 °C) and the third (295 °C) H_2O release peaks are ascribed to amidation and imidization reactions, respectively. These three water-releasing reactions are endothermic (Figure 1b). In the imidization of PMA-MA supermolecule, PMA and MA first react to form an amide structure releasing one molecule water. The formed amide structures further react to form imide structures releasing the second water molecule (Figure S3, Supporting Information). The amide and imide structures enable PMA-MA supermolecule to be highly thermostable and carbonizable.[41,42] After the imidization process, there is some edge-locating unimidized carboxylic acid (C(O)OH) and amine (NH_2) groups (Figure S4, Supporting Information) due to the slow reaction kinetics of imidization. The unimidized C(O)OH groups decompose (shown in the schematic in Figure 1e) around 483 °C (indicated by the CO_2 release peaks in Figure 1d), which results in the exfoliation of 3D-NTC by the released pyrolysis gases,[43] and the final formation of laminar nanosheet frameworks of 3D-NTCs. The decomposition of *s*-triazine structure in MA with the releasing of $NCNH_2$ (Figure 1e) at higher temperatures around 520 °C (verified by the TGA-FTIR in Figure S5, Supporting Information) may result in the formation of edge-nitrogen defect structures in 3D-NTC. The different decomposition temperatures of C(O)OH and *s*-triazine (Figure 1c; Figure S5, Supporting Information) demonstrate that in the amide and imide structure formed by amidation and imidization of PMA and MA, the pristine structure of PMA is less stable than MA (Figure 1c; Figure S5, Supporting Information). The high-nitrogen concentration in MA (67.7 at% with respect to total carbon and nitrogen atoms) and the high thermostability of amide and imide structures formed in pre-carbonization process could result in highly NTC structures. On the one hand, since the *s*-triazine structure is more stable than PMA, the 3D-NTC may have a higher nitrogen doping level compared with other carbonaceous materials prepared ~~from~~ pyrolysis methods. On the other hand, the release of $NCNH_2$ may create defective edge sites for nitrogen dopants, which enables most doped nitrogen atoms to be of edge-nitrogen configurations.

The laminar sheet-like framework and the turbostratic crystalline structure in 3D-NTC750 are shown by electron microscopy characterizations (**Figure 2**). The 3D-NTC750 sample shows laminar frameworks consisting of thin carbon nanosheets, as shown in the scanning electron microscopy (SEM) image in Figure 2a. The thickness of the carbon sheets of 3D-NTC750 obtained by transmission electron microscopy (TEM) image (Figure 2b) is around 7–12 nm (Figure S6, Supporting Information). The crystalline structure of 3D-NTC750 is

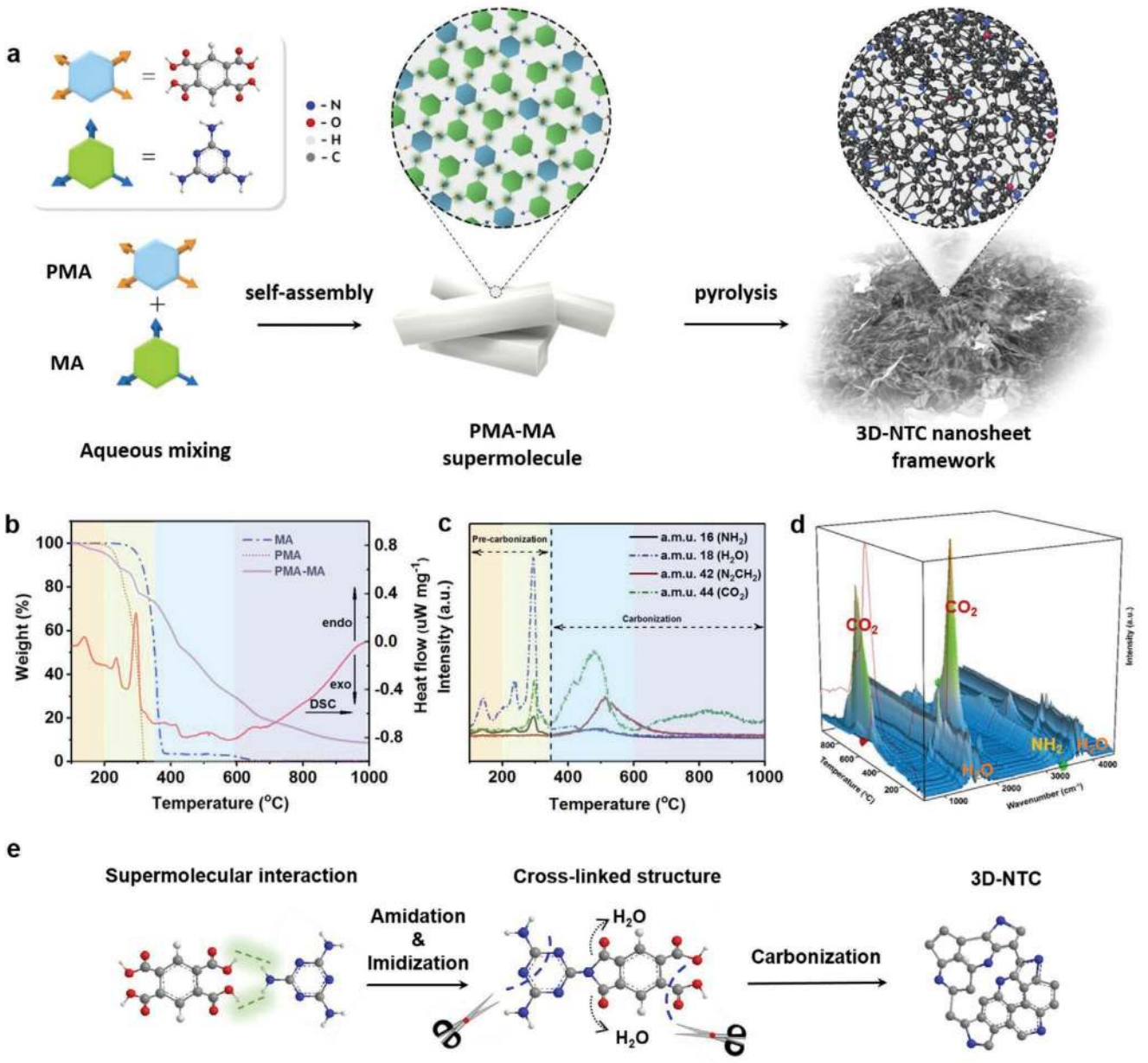

Figure 1. a) Schematic diagram showing the direct pyrolysis supermolecule strategy for the synthesis of 3D-NTC PIB anodes. Structural evolution and reactions during the pyrolysis of PMA-MA supermolecule. b) TGA and DSC curves of MA, PMA, and PMA-MA supermolecule. c) Temperature-dependent MS of PMA-MA supermolecule. d) Temperature-dependent FTIR spectra of the decomposition species from the pyrolysis of PMA-MA supermolecule. e) The schematic diagram for the pyrolysis mechanism of PMA-MA supermolecule.

turbostratically amorphous, with most defect spacings ranging from 4.4 to 5.2 Å, while a small number of defect spacings of 3.5 Å can be observed (Figure 2c). The high-resolution TEM (HRTEM) image shows many defect edge sites (Figure 2c and its inset) that result from the breakage of chemical bonds in the original PMA or MA structures, as demonstrated by the TGA-MS study. The turbostratically amorphous structure of 3D-NTC750 with large defect size could facilitate the (de) potassiation process. SEM and TEM images of 3D-NTC900 (Figure 2d,e) also show 3D laminar frameworks similar to 3D-NTC750. However, different from 3D-NTC750, 3D-NTC900 shows developed long-range ordered GNDs observed in its HRTEM (Figure 2f). The developed long-range ordered GNDs of 3D-NTC900 originates from the higher annealing temperature.[14] The GND of 3D-NTC900 is of turbostratic structure with a wide distribution of interlayer spacing (Figure 2f), which is beneficial for the diffusion of potassium ion into a carbon matrix from where GND has large interlayer spacing. Nitrogen is successfully doped in the carbon lattice of 3D-NTC750 as demonstrated by energy-dispersive X-ray spectroscopy (EDS) mapping (Figure 2g–j). To demonstrate this imidization-assisted pyrolysis is a new general strategy that can be generally

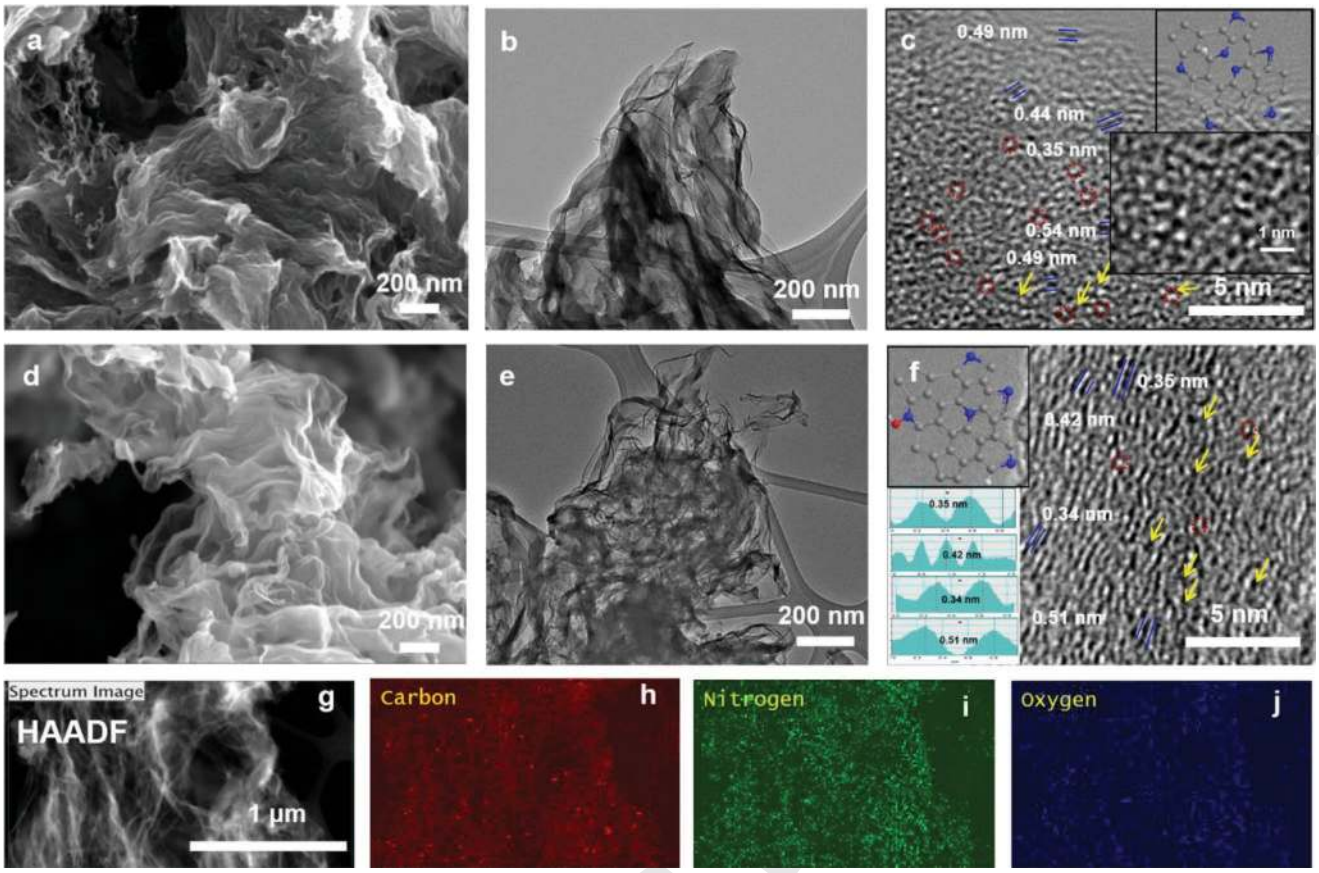

Figure 2. Electron microscopy characterization of 3D-NTCs. a) SEM, b) TEM, and c) HRTEM images of 3D-NTC750. Inset of (c) shows a typical atom-scale defect-rich structure of 3D-NTC750 and its structural schematic diagram. d) SEM, e) TEM, and f) HRTEM images of 3D-NTC900. The inset of (f) shows the structural schematic diagram of 3D-NTC900 and its contrast profiles. The red dash circles in (c) and (f) show some edge-atoms, while the yellow arrows show some defects. g) High-angle annular dark-field image (HAADF) of 3D-NTC750. EDS mapping of 3D-NTC750 with elements of h) carbon i) nitrogen, and j) oxygen.

extended to prepare other 3D-NTCs using MA and easy-accessible carboxylic acids, we prepared 3D-NTCs using MA and three general carboxylic acids such as poly(acrylic acid) (PAA), terephthalic acid (benzene-1,4-dioic acid) (BDC), and citric acid (CA). These carboxylic acids form amide structures with MA. The thermostable amide structure enables the successful preparation of 3D-NTCs. The laminar frameworks and turbostratic crystalline structures of 3D-NTC750PAA, 3D-NTC750BDC, and 3D-NTC750PAA were confirmed by multiple physicochemical techniques, such as SEM (Figure S7, Supporting Information), TEM, HRTEM (Figure S8, Supporting Information), XRD, and Raman (Figure S9, Supporting Information). These results demonstrate that our approach constitutes a general strategy that can be extended to various carboxylic acids and amines for preparing a series of edge-nitrogen-doped turbostratic carbons.

The (002) ~~broad~~ hump peaks of 3D-NTCs centering at 26.5° (**Figure 3**a) demonstrate that 3D-NTCs do not have well-defined interlayer spacing, which agrees well with the HRTEM study. The precise crystalline structures of 3D-NTCs cannot be resolved by XRD,[44] as demonstrated by their HRTEM images. The *R*-value, introduced by Dahn and co-workers,[45] to a certain extent, can be used as an indicator to reflect the order degree of amorphous carbons. The much higher *R*-value of 3D-NTC900 (4.5) than that of 3D-NTC750 (2.36) demonstrates its better graphitic structure, which is in accordance with the HRTEM study. The high I_D/I_G ratios of 0.99 for 3D-NTC750 and 0.94 for 3D-NTC900 obtained from Raman spectra (Figure 3b) imply their amorphous structural nature.[46] The pore size distribution and Brunauer–Emmett–Teller (BET) surface areas of 3D-NTCs were evaluated by argon adsorption/desorption isotherms (Figure S10, Supporting Information). The 3D-NTC750 sample has a small BET surface area of 9.26 $m^2\ g^{-1}$ and an average pore size of 5.24 nm. The 3D-NTC900 sample has a relatively larger BET surface area of 23.2 $m^2\ g^{-1}$ and a smaller average pore size of 4.87 nm, respectively (Table S1, Supporting Information). Both 3D-NTC750 and 3D-NTC900 are mesoporous carbons with layer-structured pores and wide mesopore-dominated pore size distributions from 2 to 80 nm (Figure 3c), which is in line with the SEM and TEM characterizations. The mesoporous structure of 3D-NTCs could enable fast electrolyte diffusion in the electrode.[47] The low BET specific surface areas of 3D-NTCs could reduce parasitic reactions and improve their initial Coulombic efficiencies (ICEs) towards practical PIB anodes. The nitrogen doping levels of 3D-NTCs were tested by X-ray photoelectron spectroscopy (XPS) analysis. Surprisingly, the 3D-NTC750 sample shows an unexpected ultrahigh nitrogen doping level

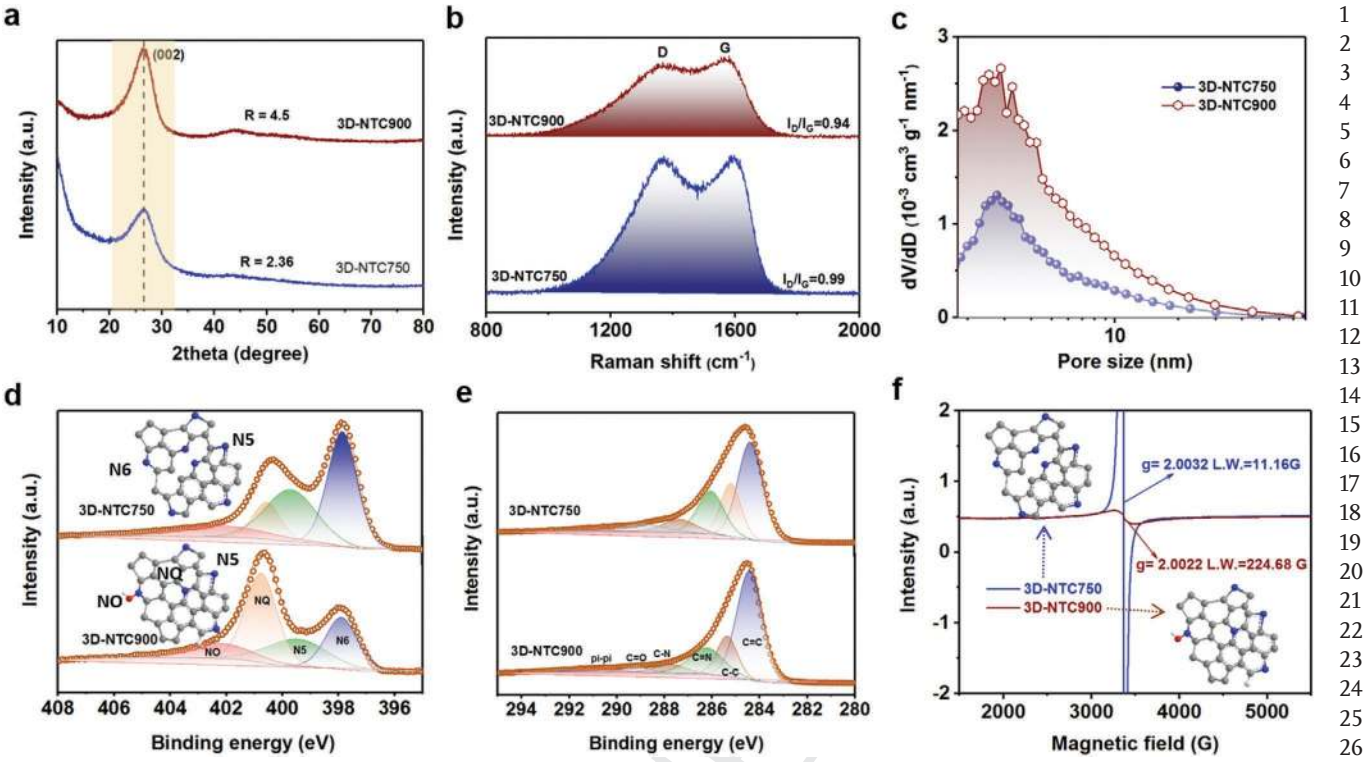

Figure 3. Physicochemical characterization of 3D-NTC. a) XRD patterns. b) Raman spectra. c) Pore size distribution. d) N 1s high-resolution XPS spectra. e) C 1s high-resolution XPS spectra. f) EPR spectra. Insets in (d) and (f) schematic show the structures of 3D-NTC750 and 3D-NTC900.

of 22.8 at% (Figure S11 and Table S2, Supporting Information). The result of CHNS elemental analysis is comparable to XPS results, which confirms the validity of XPS results. A higher nitrogen-to-carbon ratio obtained through the CHNS analysis (32.80%) compared with that through XPS analysis (30.65%) reflects the higher nitrogen content in the bulk than that on the surface of carbon matrix. This ultrahigh nitrogen doping level has rarely been reported previously. The nitrogen doping level of 3D-NTC750 was also confirmed by FTIR (Figure S12, Supporting Information) and TGA (Figure S13, Supporting Information) analyses. The ultrahigh nitrogen doping level of 3D-NTC750 results from the formation of stable amide and imide structures, and the high nitrogen content in MA molecules. The other reason for this ultrahigh nitrogen doping level of 3D-NTC750 is that PMA is less stable than MA, which indicates that MA may contribute more in the final carbon matrix of 3D-NTC750. The 3D-NTC900 sample shows lower nitrogen doping level of 9.9 at% (Table S2, Supporting Information) that is still higher than most recently reported nitrogen-doped amorphous carbons. The nitrogen bonding was analyzed by fitting N 1s XPS spectra deconvoluted into different configurations of pyridinic (N6), pyrrolic (N5), graphitic (NQ), and oxidized (NO) nitrogen (Figure 3d). The relative ratios of N6, N5, NQ, and NO for the 3D-NTC750 sample are 41.44%, 32.41%, 12.73%, and 13.42%, respectively (Table S3, Supporting Information). The corresponding values for the 3D-NTC900 sample are 23.38%, 23.15%, 39.73%, and 13.75%, respectively (Table S3, Supporting Information). The edge-nitrogen doping (N6 and N5) ratio of 3D-NTC750 is as high as ~~73.85~~%, which is attributed to the unique decomposition modality of PMA-MA supermolecule. The 3D-NTC900 sample shows a lower edge-nitrogen ratio of 46.53%, which is attributed to the fact that most edge-nitrogen configurations decompose or form in-plane graphitic nitrogens at high annealing temperature.[31] The 3D-NTC750 sample has an ultrahigh edge-nitrogen doping level of 16.8 at%. The ultrahigh edge-nitrogen doping in 3D-NTC750 could contribute to high potassium-ion storage capacity and provide facile intercalation pathways. The carbon bonding was analyzed by fitting C 1s spectra (Figure 3e). The 3D-NTC900 sample shows a high sp^2 C=C ratio due to the formation of developed GNDs (Table S4, Supporting Information).[46] The edge-nitrogen doping effect was further studied by electron paramagnetic resonance (EPR) spectroscopy (Figure 3f). The 3D-NTC750 and 3D-NTC900 exhibit Lorentzian EPR lines centering at different *g* values of 2.0032 and 2.0022, respectively. The line width (LW) of the 3D-NTC750 sample is 11.16 G, while the LW of the 3D-NTC900 sample is 224.68 G. The low LW of 3D-NTC750 indicates that the unpaired electrons ~~in 3D-NTC750~~ are more localized compared with the delocalized unpaired electrons in 3D-NTC900, which is ascribed to ~~the existence of~~ higher concentration of edge-nitrogen dopants and smaller GNDs compared with 3D-NTC900. The higher *g*-value of 2.0032 for 3D-NTC750 than the 2.0022 for 3D-NTC900 implies a strong nitrogen doping effect. Through EPR spectra, we learn that 3D-NTC750 ~~is of~~ edge-nitrogen doping configurations that separate its carbon matrix into small GNDs. The unique ultrahigh edge-nitrogen doped structure of 3D-NTC750 agrees well with the HRTEM, XPS, and TGA-MS studies. The GNDs of 3D-NTC900 develop into large sizes due to the high annealing temperatures. The high-edge-nitrogen doping of 3D-NTC750 could enhance the

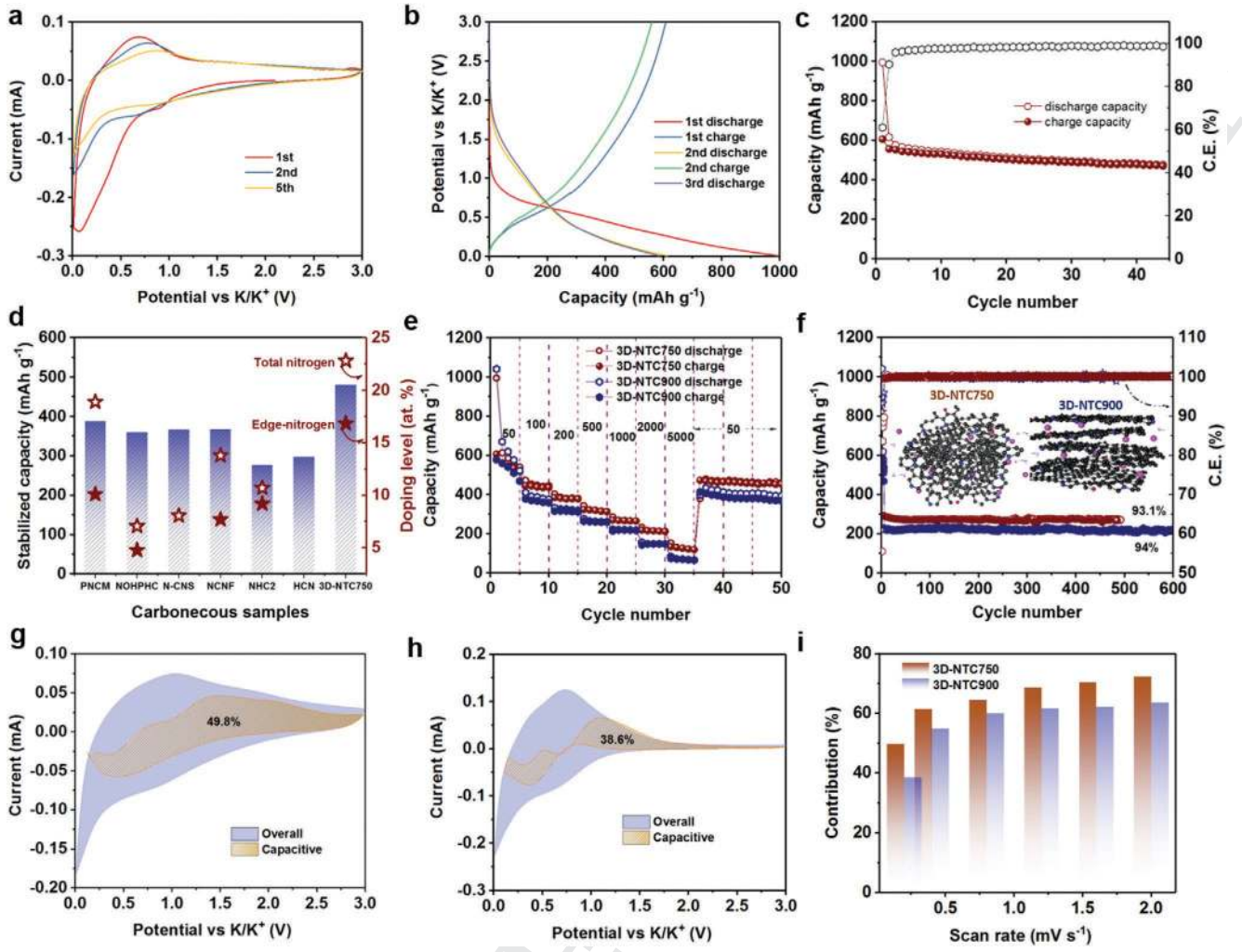

Figure 4. Electrochemical performance characterization of 3D-NTC. a) CV curves of 3D-NTC750. b) GCD curves of 3D-NTC750. c) GCD cycling of 3D-NTC750 at a current density of 50 mA g^{-1}. d) Comparison of the total nitrogen doping levels, edge-nitrogen doping levels, and the stabilized reversible capacities between 3D-NTC750 and reported high-performance anodes. e) Rate performances of 3D-NTC. f) Long-term GCD cycling stabilities of 3D-NTC at a current density of 1000 mA g^{-1}. Capacitive contributions of g) 3D-NTC750 and h) 3D-NTC900 at a scan rate of 0.2 mV s^{-1}. i) Capacitive contributions of 3D-NTCs as a function of scan rate.

potassium adsorption capacity, while the small GND could enhance the rate performances of 3D-NTC750. The well-developed GNDs in 3D-NTC900 could contribute to higher intercalation capacity compared with 3D-NTC750.

The electrochemical performances of the 3D-NTC750 electrode were first studied by cyclic voltammetry (CV). The cathodic peak starting from ≈0.7 V is attributed to the formation of solid electrolyte interphase. After the first cycle CV, the CV curves become increasingly stabilized, which indicates that the capacity decreases during the several initial cycles (**Figure 4**a). The slightly decreased current responses of the anodic and cathodic peaks in the initial cycles are ascribed to the structural rearrangement during (de)potassiation.[14] Galvanostatic charge-discharge (GCD) analysis was used to evaluate their potassium-ion storage capabilities (Figure 4b). At a current density of 50 mA g^{-1}, the 3D-NTC750 electrode displays an initial discharge capacity of 995 mAh g^{-1}, while its initial charge capacity is around 606 mAh g^{-1}. The corresponding ICE of 3D-NTC750 is 61% that is comparable to the highest values for carbonaceous PIB anodes reported in recent years.[48,49] The capacity of 3D-NTC electrode decreases in the initial cycles at a current density of 50 mA g^{-1}, and then stabilizes after 10 cycles (Figure 4c). The 3D-NTC900 electrode shows a lower first charge capacity of 578 mAh g^{-1} with a lower discharge plateau (Figure S14, Supporting Information), which is ascribed to its well-developed GNDs in its carbon skeleton. The well-developed GNDs in the 3D-NTC900 electrode endow it with a ≈100 mAh g^{-1} higher intercalation capacity than 3D-NTC750 (Figure S15, Supporting Information). The 3D-NTC prepared at a lower annealing temperature of 550 °C shows a slope GCD curve and a lower reversible capacity compared with 3D-NTC750 and 3D-NTC950 (Figure S16, Supporting Information), which is caused by its incomplete carbonization.[32] The 3D-NTC750 electrode shows an ultrahigh capacity due to its ultrahigh edge-nitrogen doping of 16.8 at% that is effective for the adsorption and

desorption of potassium ions. The intercalation-adsorption mechanism for the potassiation of 3D-NTC750 is demonstrated by EDS elemental mapping (Figures S17 and S18, Supporting Information). The atomic ratios of nitrogen, edge-nitrogen doping, and stabilized reversible capacity of 3D-NTC750 electrode are the highest among recently reported carbonaceous anodes for PIB (Figure 4d). It is necessary to note that some literature also reports high nitrogen doping, such as PNCM (18.9 at%),[33] or high edge-nitrogen doping, such as NHC2-NH_3/Ar (9.2 at%).[30] We show an example that 3D-NTC750 can achieve both high nitrogen doping (22.8 at%) and high edge-nitrogen doping (16.8 at%) levels. Both 3D-NTC750 and 3D-NTC900 show high-rate capability (the corresponding GCD curves are displayed in Figure S19, Supporting Information). The 3D-NTC750 electrode displays a high-rate capability. The 3D-NTC750 electrode displays capacities of 518, 436, 378, 313, 265, 212, and 119 mAh g^{-1} at current densities of 50, 100, 200, 500, 1000, 2000, and 5000 mA g^{-1}, respectively. After the current density is switched back to 50 mA g^{-1}, the capacity recovers to 473 mAh g^{-1}, which demonstrates its high reversibility. The 3D-NTC900 displays capacities of 469, 358, 310, 260, 216, 147, 66 mAh g^{-1} at current densities of 50, 100, 200, 500, 1000, 2000, and 5000 mA g^{-1}, respectively. The capacity of 3D-NTC900 recovers to 413 mAh g^{-1}, after the GCD current density is switched back to 50 mA g^{-1}. The long-term cycling stabilities of 3D-NTCs electrodes were tested at a current density of 1000 mA g^{-1} (Figure 4f). These 3D-NTC//K half cells failed at the 500th and 600th GCD cycles due to the potassium dendrite puncture through the separator. The 3D-NTC750 electrode displays a high capacity retention of 93.1% after 500 GCD cycles. The 3D-NTC900 electrode shows a high capacity retention of 94% after 600 cycles. Further, the 3D-NTC750 electrodes show undamaged skeletons before and after GCD cycling test (Figure S20, Supporting Information), which demonstrates the high structural stability of 3D-NTC750 during repeated (de)potassiation. The 3D-NTC750 electrode shows high ICE, high capacity, high rate capability, and high cycling stability compared with the most-recently reported carbonaceous anodes (Table S5, Supporting Information). The capacitive contribution was calculated based on Dunn's method (Figure 4g,h).[14] We find that the 3D-NTC750 electrode has a higher capacitive contribution of 49.8% than the 3D-NTC900 electrode (38.6%) at a scan rate of 0.2 mV s^{-1}. The capacitive contributions calculated at different scan rates confirm the same trend (Figure 4i). The power-law relationship of the current response and scan rate in a CV test is described as $i = av^b$.[50,51] A b value of 1 is an indicator of a surface-dominated capacitive process; whereas, a b value of 0.5 indicates the electrochemical reaction is controlled by semi-infinite diffusion. To compare the different kinetics of 3D-NTC electrodes, the b values of 3D-NTC electrodes were calculated based on the CV curves obtained at different scan rates (Figure S21, Supporting Information). The 3D-NTC750 electrode exhibits higher b values of 0.751 and 0.612 for anodic and cathodic peaks, respectively, compared with 3D-NTC900 (b values are 0.703, 0.562) (Figure S22, Supporting Information). The higher capacitive contributions and higher b values of 3D-NTC750 result from the undeveloped GNDs and large defect spacing, which enables fast potassium adsorption and desorption. The 3D-NTC900 electrode has smaller interlayer spacing that may impede the diffusion of potassium ions. The above results demonstrate that our ultrahigh edge-nitrogen doped 3D-NTC750 has both high K-ion storage capacity and rate capability. To further interpret our experimental results, we performed a theoretical study of the K-adsorption capability on different defective configurations with N dopant and tri-vacancy based on density functional theory. Three defective configurations (pyridinic nitrogen (N6), pyrrolic nitrogen (N5), and tri-vacancy) (Figure S23, Supporting Information) were modeled in bilayer graphene to compare with graphitic nitrogen (NQ) doped and undoped graphenes. The edge-nitrogen configurations (N5 and N6) show unambiguously higher adsorption energy (E_a) than NQ doped and undoped graphenes (Figure S24, Supporting Information). The tri-vacancy structure was obtained by replacing the N6 dopant with a carbon atom. It shows slightly lower E_a than the N6 structure (Figure S24, Supporting Information), which indicates that both the carbon-vacancy-induced and edge-nitrogen-induced vacancy defects can enhance the K-adsorption capability.[31] In other words, the capacity enhancement of nitrogen-doped carbons could be related to both edge-nitrogen doping and carbon-vacancy-induced defects. 3D-NTC750 has a lower graphitization and higher edge-nitrogen doping level than 3D-NTC900, which results in more edge-nitrogen-induced vacancy defects and higher E_a. As a result, 3D-NTC750 has a higher surface-dominated adsorption capacity than 3D-NTC900. We calculated the charge density difference to understand the bonding nature of the adsorbed K atoms (Figure S25, Supporting Information). In all the defective configurations, there is a net electron transfer between K and nearest carbon atoms, which suggests an ionic nature of the bonding. The charge density tends to accumulate around the N5 and N6 edge-nitrogen dopants, which proves the effectiveness of our edge-nitrogen doping strategy.

The 3D-NTC750 electrode was further assembled into a 3D-NTC750//PTCDA PIB full cell using the PTCDA cathode (schematic diagram shown in **Figure 5**a). The PTCDA cathode shows a capacity of ≈120 mAh g^{-1} as a PIB cathode (Figure S26, Supporting Information).[52,53] A 4.5 V LED can be lit by two PIB full cells in series (Figure 5b). The 3D-NTC750//PTCDA PIB full cell shows a reversible symmetric CV behavior (Figure S27, Supporting Information). Besides, the 3D-NTC750//PTCDA PIB full cell displays a decent rate performance and high operational voltages at various GCD current densities ranging from 30 to 200 mA g^{-1} (Figure 5c,d). The cycling performance of PIB full cell was tested under a current density of 200 mA g^{-1}. After 100 GCD cycles, the PIB full cell can still deliver a high capacity of 241 mAh g^{-1} (Figure 5e). The cycling stability of this 3D-NTC750//PTCDA PIB full cell could be further enhanced by optimizing the electrolyte compositions.[52] The self-discharge rate of this PIB full cell (Figure S28, Supporting Information) was provided as a reference to other laboratory-made coin-cell PIB full cells. 3D-NTC750//PTCDA PIB full cell shows a slow self-discharge rate of 0.088% per hour. The 3D-NTC750//PTCDA PIB full cell delivers an energy density of 187 Wh kg^{-1} (Figure S29, Supporting Information) that is among the best values reported for PIB full cells (Figure 5f). The energy density of 3D-NTC750//PTCDA PIB is higher than recently reported

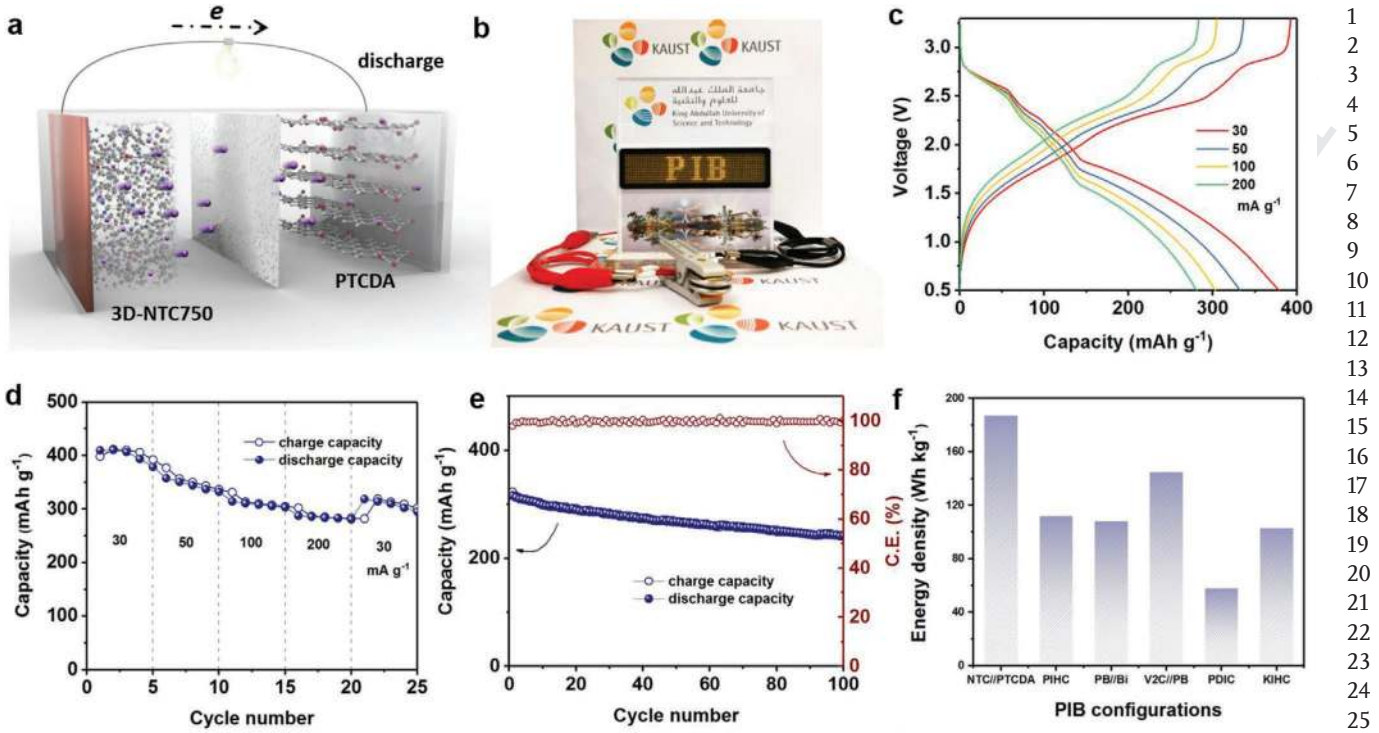

Figure 5. Electrochemical performances of 3D-NTC750//PTCDA PIB full cell. a) A schematic diagram of PIB full cell. b) An LED light showing "PIB" driven by two PIB full cells. c) GCD curves at different current densities and d) the rate capability. e) The cycling performance of PIB full cell at a current density of 200 mA g^{-1}. The capacity was calculated based on the mass of anode. f) Comparison of energy density with other PIB configurations reported in the literature.

PIBs and potassium ion capacitors, such as PIHC,[20] PB//Bi,[54] V2C//PB,[55] PDIC,[56] and KIHC.[57]

In summary, we have developed a new, general strategy of direct pyrolysis of supermolecules to synthesize carbonaceous anodes with ultrahigh edge-nitrogen doping for PIBs. The optimized carbon anodes show a turbostratically amorphous structure with an ultrahigh nitrogen doping level of 22.8 at% and an ultrahigh edge-nitrogen doping level of 16.8 at%. The ultrahigh edge-nitrogen doping and unique defect-rich turbostratic structures of our carbon anodes result in ~~their~~ remarkable performances as PIB anodes. Our new synthesis strategy can be extended to prepare a family of highly edge-nitrogen-doped carbonaceous materials for other alkali-metal ion batteries.

Supporting Information

Supporting Information is available from the Wiley Online Library or from the author.

Acknowledgements

The research reported in this publication was supported by the King Abdullah University of Science and Technology. The authors thank the Core Laboratories at KAUST for their excellent support.

Conflict of Interest

The authors declare no conflict of interest.

Keywords

active sites, anode, carbon, nitrogen doping, potassium-ion battery

Received: February 1, 2020
Revised: April 22, 2020
Published online:

[1] D. Larcher, J. M. Tarascon, *Nat. Chem.* **2015**, *7*, 19.
[2] C. Vaalma, D. Buchholz, M. Weil, S. Passerini, *Nat. Rev. Mater.* **2018**, *3*, 18013.
[3] W. Zhang, F. Zhang, F. Ming, H. N. Alshareef, *EnergyChem* **2019**, *1*, 100012.
[4] J. Y. Hwang, S. T. Myung, Y. K. Sun, *Adv. Funct. Mater.* **2018**, *28*, 1802938.
[5] L. Jiang, Y. Lu, C. Zhao, L. Liu, J. Zhang, Q. Zhang, X. Shen, J. Zhao, X. Yu, H. Li, X. Huang, L. Chen, Y.-S. Hu, *Nat. Energy* **2019**, *4*, 495.
[6] W. Zhang, Y. Liu, Z. Guo, *Sci. Adv.* **2019**, *5*, eaav7412.
[7] H. Kim, J. C. Kim, M. Bianchini, D. H. Seo, J. Rodriguez-Garcia, G. Ceder, *Adv. Energy Mater.* **2018**, *8*, 1702384.
[8] I. Sultana, M. M. Rahman, Y. Chen, A. M. Glushenkov, *Adv. Funct. Mater.* **2018**, *28*, 1703857.
[9] Z. Jian, Z. Xing, C. Bommier, Z. Li, X. Ji, *Adv. Energy Mater.* **2016**, *6*, 1501847.
[10] X. Yao, Y. Ke, W. Ren, X. Wang, F. Xiong, W. Yang, M. Qin, Q. Li, L. Mai, *Adv. Energy Mater.* **2019**, *9*, 1803260.
[11] S. Komaba, T. Hasegawa, M. Dahbi, K. Kubota, *Electrochem. Commun.* **2015**, *60*, 172.
[12] Z. Jian, W. Luo, X. Ji, *J. Am. Chem. Soc.* **2015**, *137*, 11566.
[13] W. Luo, J. Wan, B. Ozdemir, W. Bao, Y. Chen, J. Dai, H. Lin, Y. Xu, F. Gu, V. Barone, L. Hu, *Nano Lett.* **2015**, *15*, 7671.

[14] W. Zhang, J. Ming, W. Zhao, X. Dong, M. N. Hedhili, P. M. F. J. Costa, H. N. Alshareef, *Adv. Funct. Mater.* **2019**, *29*, 1903641.
[15] Y. Cao, L. Xiao, M. L. Sushko, W. Wang, B. Schwenzer, J. Xiao, Z. Nie, L. V. Saraf, Z. Yang, J. Liu, *Nano Lett.* **2012**, *12*, 3783.
[16] X. Wu, Y. Chen, Z. Xing, C. W. K. Lam, S. Pang, W. Zhang, Z. Ju, *Adv. Energy Mater.* **2019**, *9*, 1900343.
[17] G. Li, B. Huang, Z. Pan, X. Su, Z. Shao, L. An, *Energy Environ. Sci.* **2019**, *12*, 2030.
[18] B. Cao, Q. Zhang, H. Liu, B. Xu, S. Zhang, T. Zhou, J. Mao, W. K. Pang, Z. Guo, A. Li, J. Zhou, X. Chen, H. Song, *Adv. Energy Mater.* **2018**, *8*, 1801149.
[19] J. Liu, T. Yin, B. Tian, B. Zhang, C. Qian, Z. Wang, L. Zhang, P. Liang, Z. Chen, J. Yan, X. Fan, J. Lin, X. Chen, Y. Huang, K. P. Loh, Z. X. Shen, *Adv. Energy Mater.* **2019**, *9*, 1900579.
[20] J. Chen, B. Yang, H. Hou, H. Li, L. Liu, L. Zhang, X. Yan, *Adv. Energy Mater.* **2019**, *9*, 1803894.
[21] H. He, D. Huang, Y. Tang, Q. Wang, X. Ji, H. Wang, Z. Guo, *Nano Energy* **2019**, *57*, 728.
[22] X. Lin, J. Huang, B. Zhang, *Carbon* **2019**, *143*, 138.
[23] J. Ding, H. Zhang, H. Zhou, J. Feng, X. Zheng, C. Zhong, E. Paek, W. Hu, D. Mitlin, *Adv. Mater.* **2019**, *31*, 1900429.
[24] J. Yang, Z. Ju, Y. Jiang, Z. Xing, B. Xi, J. Feng, S. Xiong, *Adv. Mater.* **2018**, *30*, 1700104.
[25] X. Zhou, L. Chen, W. Zhang, J. Wang, Z. Liu, S. Zeng, R. Xu, Y. Wu, S. Ye, Y. Feng, X. Cheng, Z. Peng, X. Li, Y. Yu, *Nano Lett.* **2019**, *19*, 4965.
[26] L. Liu, Y. Chen, Y. Xie, P. Tao, Q. Li, C. Yan, *Adv. Funct. Mater.* **2018**, *28*, 1801989.
[27] D. Qiu, J. Guan, M. Li, C. Kang, J. Wei, Y. Li, Z. Xie, F. Wang, R. Yang, *Adv. Funct. Mater.* **2019**, *29*, 1903496.
[28] D. S. Bin, X. J. Lin, Y. G. Sun, Y. S. Xu, K. Zhang, A. M. Cao, L. J. Wan, *J. Am. Chem. Soc.* **2018**, *140*, 7127.
[29] J. Ruan, F. Mo, Z. Chen, M. Liu, S. Zheng, R. Wu, F. Fang, Y. Song, D. Sun, *Adv. Energy Mater.* **2020**, *10*, 1904045.
[30] W. Yang, J. Zhou, S. Wang, W. Zhang, Z. Wang, F. Lv, K. Wang, Q. Sun, S. Guo, *Energy Environ. Sci.* **2019**, *12*, 1605.
[31] Y. Xu, C. Zhang, M. Zhou, Q. Fu, C. Zhao, M. Wu, Y. Lei, *Nat. Commun.* **2018**, *9*, 1720.
[32] W. Zhang, Z. Cao, W. Wang, E. Alhajji, A. H. Emwas, P. M. F. J. Costa, L. Cavallo, H. N. Alshareef, *Angew. Chem., Int. Ed.* **2020**, *59*, 4448.
[33] Y. Xie, Y. Chen, L. Liu, P. Tao, M. Fan, N. Xu, X. Shen, C. Yan, *Adv. Mater.* **2017**, *29*, 1702268.
[34] Y. Liu, C. Yang, Q. Pan, Y. Li, G. Wang, X. Ou, F. Zheng, X. Xiong, M. Liu, Q. Zhang, *J. Mater. Chem. A* **2018**, *6*, 15162.
[35] L. Zhu, R. Peng, X. Ren, Q. Ai, Y. Liu, J. Feng, P. Si, Q. Sun, J. Lou, D. Li, L. Ci, Z. Liang, *Adv. Energy Mater.* **2018**, *8*, 1802386.
[36] P. Li, J. Hwang, *J. Mater. Chem. A* **2018**, *6*, 12551.
[37] Y. Li, C. Yang, F. Zheng, X. Ou, Q. Pan, Y. Liu, G. Wang, *J. Mater. Chem. A* **2018**, *6*, 17959.
[38] Z. Liu, L. Zhang, L. Sheng, Q. Zhou, T. Wei, J. Feng, Z. Fan, *Adv. Energy Mater.* **2018**, *8*, 1802042.
[39] J. C. Swarbrick, B. L. Rogers, N. R. Champness, P. H. Beton, *J. Phys. Chem. B* **2006**, *110*, 6110.
[40] S. C. Yan, Z. S. Li, Z. G. Zou, *Langmuir* **2009**, *25*, 10397.
[41] J. Gu, Z. Du, C. Zhang, S. Yang, *Adv. Energy Mater.* **2016**, *6*, 1600917.
[42] Z. Xu, X. Zhuang, C. Yang, J. Cao, Z. Yao, Y. Tang, J. Jiang, D. Wu, X. Feng, *Adv. Mater.* **2016**, *28*, 1981.
[43] S. Y. Lu, M. Jin, Y. Zhang, Y. B. Niu, J. C. Gao, C. M. Li, *Adv. Energy Mater.* **2018**, *8*, 1702545.
[44] X. Dou, I. Hasa, D. Saurel, C. Vaalma, L. Wu, D. Buchholz, D. Bresser, S. Komaba, S. Passerini, *Mater. Today* **2019**, *23*, 87.
[45] Y. Liu, J. S. Xue, T. Zheng, J. R. Dahn, *Carbon* **1996**, *34*, 193.
[46] W. Zhang, Y. Lei, F. Ming, Q. Jiang, P. M. F. J. Costa, H. N. Alshareef, *Adv. Energy Mater.* **2018**, *8*, 1801840.
[47] H. Li, Z. Cheng, Q. Zhang, A. Natan, Y. Yang, D. Cao, H. Zhu, *Nano Lett.* **2018**, *18*, 7407.
[48] L. Fan, K. Lin, J. Wang, R. Ma, B. Lu, *Adv. Mater.* **2018**, *30*, 1800804.
[49] L. Fan, R. Ma, Q. Zhang, X. Jia, B. Lu, *Angew. Chem., Int. Ed.* **2019**, *58*, 10500.
[50] Y. Liu, Y. X. Lu, Y. S. Xu, Q. S. Meng, J. C. Gao, Y. G. Sun, Y. S. Hu, B. B. Chang, C. T. Liu, A. M. Cao, *Adv. Mater.* **2020**, 2000505.
[51] B. Lee, M. Kim, S. Kim, J. Nanda, S. J. Kwon, H. D. Jang, D. Mitlin, S. W. Lee, *Adv. Energy Mater.* **2020**, 1903280.
[52] L. Fan, R. Ma, J. Wang, H. Yang, B. Lu, *Adv. Mater.* **2018**, *30*, 1805486.
[53] Y. Chen, W. Luo, M. Carter, L. Zhou, J. Dai, K. Fu, S. Lacey, T. Li, J. Wan, X. Han, Y. Bao, L. Hu, *Nano Energy* **2015**, *18*, 205.
[54] K. Lei, C. Wang, L. Liu, Y. Luo, C. Mu, F. Li, J. Chen, *Angew. Chem., Int. Ed.* **2018**, *57*, 4687.
[55] F. Ming, H. Liang, W. Zhang, J. Ming, Y. Lei, A.-H. Emwas, H. N. Alshareef, *Nano Energy* **2019**, *62*, 853.
[56] Y. Feng, S. Chen, J. Wang, B. Lu, *J. Energy Chem.* **2020**, *43*, 129.
[57] Y. Li, Y. Yang, P. Zhou, T. Gao, Z. Xu, S. Lin, H. Chen, J. Zhou, S. Guo, *Matter* **2019**, *1*, 893.

Q5

ADVANCED MATERIALS

Reprint Order Form 2019
- please return with your proofs -

Editorial Office:

Wiley-VCH Verlag, Boschstrasse 12
69469 Weinheim, Germany

Tel.: (+49) 6201 606 235
Fax: (+49) 6201 606 500

E-mail: advmat@wiley-vch.de
http://www.advmat.de

Manuscript No. _____

Please send me and bill me for

☐ no. of **reprints** via ☐ airmail (+ 25 Euro) ☐ surface mail

☐ no. of **copies of this issue** (1 copy: 28 Euro) via ☐ airmail (+ 25 Euro) ☐ surface mail

☐ **high-resolution PDF file** (330 Euro).
My e-mail address:

_____

Please note: It is not permitted to present the PDF file on the internet or on company homepages

★**Special Offer**★ If you order 200 or more reprints you will get a PDF file for half price.

Information regarding VAT
Please note that from German sales tax point of view, the charge for **Reprints, Issues or Posters** is considered as **"supply of goods"** and therefore, in general, such delivery is a subject to German sales tax. However, this regulation has no impact on customers located outside of the European Union. Deliveries to customers outside the Community are automatically tax-exempt. Deliveries within the Community to institutional customers outside of Germany are exempted from the German tax (VAT) only if the customer provides the supplier with his/her VAT number. The VAT number (value added tax identification number) is a tax registration number used in the countries of the European Union to identify corporate entities doing business there. It starts with a country code (e.g. FR for France, GB for Great Britain) and follows by numbers.

Mail reprints /cover posters / copies of the issue to:

_____
_____
_____
_____
_____

Invoice address:

_____
_____
_____
_____
_____

_____
Date, Signature **Stamp**

VAT no.: _____
(institutes / companies in EU countries only)

Purchase Order No.: _____

Credit Card Payment

VISA, MasterCard, AMERICAN EXPRESS
Please use the Credit Card Token Generator located at the website below to create a token for secure payment. The token will be used instead of your credit card number.

Credit Card Token Generator:
https://www.wiley-vch.de/editorial_production/index.php

Please transfer your token number to the space below.

Credit Card Token Number:

Cover Posters

Posters are available of all the published covers and frontispieces in two sizes

☐ DIN A2 42 x 60 cm / 17 x 24in (one copy: **39 Euro**)
☐ DIN A1 60 x 84 cm / 24 x 33in (one copy: **49 Euro**)

Postage for shipping posters overseas by airmail:
+ 25 Euro

Postage for shipping posters within Europe by surface mail:
+ 15 Euro

Price list for reprints (The prices include mailing and handling charges. All Wiley-VCH prices are exclusive of VAT)

No. of pages	Price (in Euro) for orders of 50 copies	100 copies	150 copies	200 copies	300 copies	500 copies
1-4	345	395	425	445	548	752
5-8	490	573	608	636	784	1077
9-12	640	739	786	824	1016	1396
13-16	780	900	958	1004	1237	1701
17-20	930	1070	1138	1196	1489	2022
for every additional 4 pages	147	169	175	188	231	315

★ **Special Offer** ★ If you order 200 or more reprints you will get a PDF file for half price.

Wiley-VCH Verlag GmbH & Co. KGaA; Location of the Company: Weinheim;
Chairman of the Supervisory Board: John Kritzmacher,
Trade Register: Mannheim, HRB 432833, General Partner: John Wiley & Sons GmbH,
Location: Weinheim, Trade Register Mannheim, HRB 432296,
Managing Directors: Sabine Steinbach, Dr. Guido F. Herrmann

WILEY-VCH